Regular Article

Experimental and numerical analysis of mass transfer in a binary mixture with Soret effect in the presence of weak convection[⋆]

Y. Gaponenko[1,2], A. Mialdun[1], and V. Shevtsova[1,a]

[1] MRC, EP CP-165/62, Université Libre de Bruxelles (ULB), av. F.D. Roosevelt, 50, Brussels, 1050 Belgium
[2] Institute of Computational Modelling SB RAS, Krasnoyarsk, 660036, Russia

Abstract. One of the targets of the experiment IVIDIL (Influence Vibrations on Diffusion in Liquids) conducted on-board ISS was to study the response of binary mixtures to vibrational forcing when the density gradient results from thermal and compositional variations. Compositional variations were created by the Soret effect and can strengthen or weaken the overall density gradient and, consequently, the response to vibrational forcing. We present the results of two experimental runs conducted on-board ISS in the frame of the experiment IVIDIL for low and strong vibrational forcing. The experimental observations revealed that a significant mean flow is set within 2 minutes after imposing vibrations and later in time it varies weakly and slowly due to the Soret effect. A mathematical model has been developed to compute the thermal and concentration fields in the experiment IVIDIL and verify the accuracy of picture processing based on the classical approach used in non-convective systems with the Soret effect. The effect of temperature and concentrations perturbations by joint action of vibrational convection and Soret effect on long time scale are carefully examined. The model demonstrates that image processing used for non-convective systems is suitable for the systems with vibration-affected thermodiffusion experiment.

1 Introduction

Thermal gradients can induce a wide range of thermal transport phenomena, mass separation in multicomponent mixtures (thermodiffusion or Soret effect), or initiate convection. When a container filled with liquid is subjected to high frequency vibrations, the fluid is not able to react due to inertia and this may create a flow. When a density gradient is present, the inertia will not be uniform, which leads to convective motion. Density gradients can be generated in a single-component fluid when a temperature difference is established across the container or in a fluid mixture where the concentration of different species is not homogeneous. The vibrational convection is fairly well understood in numerical and theoretical studies [1,2], but until very recent no experimental evidence has been made available due to the fact that buoyancy-induced flows are usually dominant over vibration-induced ones, therefore preventing their observation [3]. Thus, vibrational convection would become detectable in a reduced gravity environment. Earlier attempts to observe vibrational flows have used either a single component fluid in short-time microgravity experiments in parabolic flights [4–6] or near-critical fluids in the experiments on MIR station [7–10].

The IVIDIL experimental objectives were manifold. One of the objectives of the experiment IVIDIL (Influence Vibrations on Diffusion in Liquids) performed on the ISS was to present qualitative analysis of the mean flows in two-component mixtures. Another target was to study the influence of vibrations on the measurement of diffusion and Soret (or thermal diffusion) coefficients in binary mixtures [11–13]. A few experimental runs without imposed vibrations enabled measurements of the Soret coefficient of water-isopropanol (IPA) mixtures at two specific compositions, namely, $c = 0.50$ and $c = 0.90$ mass fraction of water [14]. Other experiments were aimed at the understanding the impact of vibrations on mass transport. Optical digital interferometry (ODI) was used to monitor the temperature and concentration fields. The recorded images were processed using a well-established procedure [15, 16]. In this approach all the temperature variations are included into the reference image and at the later time the variation of the refractive index is assigned only to the concentration field. However, the imposed vibrations cause the mean flow which may lead to the re-distribution of the temperature field at later times and, consequently, the concentration field. In the present work, an attempt is made to clarify this situation by computing temperature distributions over the total duration of the non-isothermal phase of the IVIDIL experiment and compare with experimental observations being processed in a usual way.

[⋆] Contribution to the Topical Issue "Thermal non-equilibrium phenomena in multi-component fluids" edited by Fabrizio Croccolo and Henri Bataller.

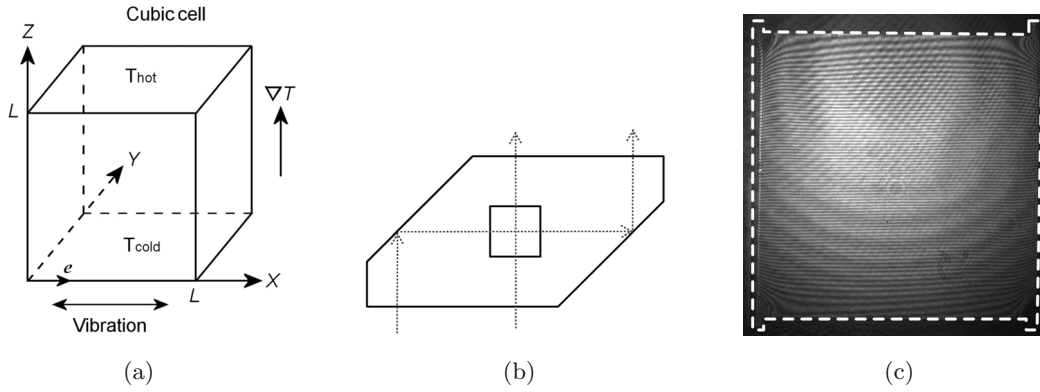[a] e-mail: `vshev@ulb.ac.be`

(a)   (b)   (c)

Fig. 1. (a) The sketch of the cell and the coordinate system. (b) External shape of the cell with two perpendicular optical paths. (c) Interference pattern of the cell. White line depicts the volume filled with liquid.

Table 1. The physical properties of the mixtures 90%water-10%IPA and 50%water-50%IPA at 25 °C: density ρ, thermal β_T and solutal β_C expansions, kinematic viscosity $\nu = \mu/\rho$, thermal diffusivity χ, diffusion D and Soret S_T coefficients, variation of a refractive index with concentration $\partial n/\partial c$ and temperature $\partial n/\partial T$.

C_0, water	ρ (kg/m^3)	β_T (10^{-3} K^{-1})	β_C	ν (10^{-6} m^2/s)	χ (10^{-7} m^2/s)	D (10^{-10} m^2/s)	S_T (10^{-3} K^{-1})	$\partial n/\partial c$ (10^{-2})	$\partial n/\partial T$ (10^{-4} K^{-1})
0.9	980.1	0.333	−0.1437	1.44	1.30	7.11	−7.4	−3.64	−3.474

The complementary target is to justify the best time moment for the choice of the reference image.

Besides the IVIDIL experiment this analysis might be of interest for other experiments related to the measurements of thermodiffusion in the presence of a very weak convection. This paper may help to answer the question whether the second diagnostic (*e.g.*, second laser) is required or not to separate contributions of the temperature and concentration.

2 The experiment

The IVIDIL cell had a cubic inner volume of $10 \times 10 \times 10 \, \mathrm{mm}^3$. The cell, coordinate system and the direction of temperature gradient are presented in fig. 1(a). The horizontal walls, let us call them as bottom and top walls according to fig. 1(a), are kept at constant temperatures T_{cold} and T_{hot}, respectively. Temperature differences, $\Delta T = T_{\mathrm{hot}} - T_{\mathrm{cold}}$, applied to the cell were 5, 10, or 15 K with a typical stability of ± 0.02 K. The external walls of the cell are shaped in the form of two prisms (see fig. 1(b)) to allow optical observation in two perpendicular directions [4]. The coherent light source was a laser diode emitting at $\lambda = 670$ nm wavelength. Along with the housekeeping data, the interferograms are the only source of scientific information provided by the IVIDIL experiment. An example of interference pattern in the front view of the cell, which is similar to the side view in the absence of vibrations, is shown in fig. 1(c). The white line, depicting the volume filled with liquid, shows grooves of 2 mm high and 0.5 mm wide. There are several reasons for these grooves and one of them is to keep a full optical view of the cell.

The result obtained after processing an interferogram is a spatial phase distribution $\Delta\varphi(x,z,t)$, which is transformed into the variation in the refractive index $\Delta n(x,z,t)$ and related to the variation in the concentration and temperature fields by the equation

$$\Delta n(x,z,t) = \frac{\lambda}{2\pi L}\Delta\varphi(x,z,t)$$
$$= \left(\frac{\partial n}{\partial T}\right)_{p,c}\Delta T(x,z,t) + \left(\frac{\partial n}{\partial c}\right)_{p,T}\Delta C(x,z,t),$$
(1)

where λ is the wavelength of the laser diode and L is the cell size. Usually, the contributions from temperature and concentration are separated in time because the diffusion time ($\tau_D = L^2/D$) is 180 times larger than thermal time ($\tau_{\mathrm{th}} = L^2/\chi$). Hereafter, we consider experiments with a mixture that had a negative Soret effect (90%water-10%IPA). The mean temperature $T_0 = (T_h + T_c)/2$, is chosen to be the reference temperature at which all the physical properties of the fluids are measured. The properties of the mixtures, which were recently measured [14], are listed in table 1.

3 Mathematical formulation

3.1 Governing equations

The working liquid is placed in a cubic cell of internal size $L = 10$ mm. Let us chose C as the mass fraction of one component in binary mixture then the mass fraction of

the other component will be $(1 - C)$. Hereafter in binary mixtures of water-isopropanol we choose C as mass fraction of water, which is the denser component, and C_0 is its initial concentration in the mixture.

When pressure diffusion is negligible, the diffusion flux $\mathbf{J}_C$ is driven by concentration and temperature gradients:

$$\mathbf{J}_C = -\rho_0[D\nabla C + D_T C(1 - C)\nabla T]$$
$$= -\rho_0 D[\nabla C + S_T C(1 - C)\nabla T]. \qquad (2)$$

Here D_T is the thermodiffusion coefficient which can be expressed via Soret coefficient $S_T = D_T/D$. The typical approximation for such a class of problems, $C(1 - C) \sim C_0(1 - C_0)$, will be used in the last term for the mass flux. The study is focused on the results in the mixture with negative Soret effect $S_T < 0$. In this case the temperature gradient and the flux due to thermal diffusion have the same direction, hence, the denser component is driven by thermal diffusion towards the hot wall.

We assume that the variations of temperature, concentration, and pressure in space and time are small. Then the mixture density does not vary significantly and the fluid can be considered to be incompressible. The density of binary mixture is assumed to be linear function of the temperature and concentration

$$\rho = \rho_0 \left(1 - \beta_T(T - T_0) - \beta_C(C - C_0)\right). \qquad (3)$$

Here $T_0 = (T_{\text{hot}} + T_{\text{cold}})/2$ is the mean temperature of the system. In convection problems, the small density variations must be taken into account in the body force term since they are the main cause of motion. Experimental study [17] revealed that viscosity of the water-isopropanol mixture strongly varies with temperature. The measured dependence of the dynamic viscosity on temperature $\mu(T)$ is presented in fig. 2(a) and described by a linearly decreasing function of temperature

$$\mu = \mu_0 \left(1 - \mu_T(T - T_0)\right),$$
$$\mu_T = -\mu_0^{-1} \partial\mu/\partial T. \qquad (4)$$

In the coordinate system associated with the cell, the acceleration applied to the system is

$$g_{os} = A\omega^2 \cos(\omega t)\,\mathbf{e},$$

where $\mathbf{e} = (1, 0, 0)$ is the unit vector along the axis of vibrations. A is the amplitude and $\omega = 2\pi f$ is the cyclic frequency of imposed vibrations.

The problem is considered in Boussinesq approximation. The validity of Boussinesq approximation in the presence of vibrations was previously discussed for several problems [1, 6, 18]. Then the equations of motion and heat and mass transport can be written as

$$\partial_t \mathbf{V} + (\mathbf{V} \cdot \nabla)\mathbf{V} = -\rho_0^{-1}\nabla P + \rho_0^{-1}\nabla \cdot (\tau)$$
$$+ [1 - \beta_T(T - T_0) - \beta_C(C - C_0)]\,A\omega^2 \cos(\omega t)\,\mathbf{e},$$
$$\partial_t T + \mathbf{V} \cdot \nabla T = \chi\nabla^2 T,$$
$$\partial_t C + \mathbf{V} \cdot \nabla C = \nabla(D(T)\nabla C) + C_0(1 - C_0)\nabla(D_T\nabla T),$$
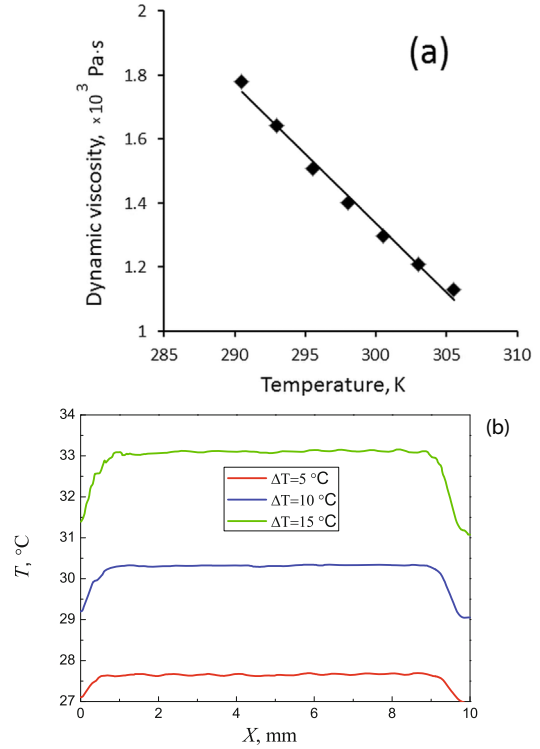$$\nabla \cdot \mathbf{V} = 0. \qquad (5)$$

Fig. 2. (a) Experimentally obtained temperature dependence of viscosity for the mixture with 90% water-10% IPA. (b) Measured temperature profiles along the hot wall for various imposed temperature differences ΔT.

Here $\mathbf{V}$ is the velocity vector, the other notations are given in the caption to table 1. For comparison with experiment the problem is solved in dimensional variable. The stress tensor τ is given by

$$\tau = \mu(T)(\nabla\mathbf{V} + \nabla\mathbf{V}^T).$$

3.2 Boundary conditions

The cell boundaries are rigid with no-slip condition for the velocity. Boundary conditions for the concentration corresponds to zero mass flux $\mathbf{J}_C = 0$ on the all solid walls,

$$\nabla C = -S_T C_0(1 - C_0)\nabla T. \qquad (6)$$

Boundary conditions for the temperature are taken from the experiment. Measurements reveal that, due to the cell design, the temperature on the limits of the cell is changed by ΔT_{corr} on the length $\delta_L \approx 0.08L$. Figure 2(b) shows the measured temperature profile along the hot wall for different ΔT. The temperature distribution along the cold wall is similar and is not shown. The boundary conditions, used in simulations, correspond to the experimental

profile:

$$z = 0 :$$

$$0 < x < \delta_L : \qquad T = T_{\text{cold}} + \Delta T_{\text{corr}} \frac{\delta_L - x}{\delta_L};$$

$$\delta_L < x < L - \delta_L : \quad T = T_{\text{cold}};$$

$$L - \delta_L < x < L : \quad T = T_{\text{cold}} + \Delta T_{\text{corr}} \frac{x - (L - \delta_L)}{\delta_L}; \quad (7)$$

$$z = L :$$

$$0 < x < \delta_L : \qquad T = T_{\text{hot}} - \Delta T_{\text{corr}} \frac{\delta_L - x}{\delta_L};$$

$$\delta_L < x < L - \delta_L : \qquad T = T_{\text{hot}};$$

$$L - \delta_L < x < L : \qquad T = T_{\text{hot}} - \Delta T_{\text{corr}} \frac{x - (L - \delta_L)}{\delta_L}. \quad (8)$$

The temperature distribution on the lateral walls is assumed to be a linear function but taking into account the temperature drop at the ends of the horizontal walls

$$x, y = 0, L : \ T = T_{\text{cold}} + \Delta T_{\text{corr}} + (\Delta T - 2\Delta T_{\text{corr}}) z/L. \quad (9)$$

The value of ΔT_{corr} was determined for each experiment and it was ranged $0.6\,\text{K} < \Delta T_{\text{corr}} < 1.25\,\text{K}$.

4 Results

4.1 Evolution of the temperature field in course of the IVIDIL experiment

In the IVIDIL experiment the temperature evolution in time can be divided in three steps which are outlined in fig. 3. Each of the steps is discussed in more detail below. The preliminary step, when a constant mean temperature $T = 298.15\,\text{K}$ was kept for $25\,\text{min}$, is not discussed here. At the first step which lasts $10\,\text{min}$, a temperature difference ΔT was imposed between the horizontal walls of the experimental cubic cell. The approach of a temperature field to a steady state is described by the relaxation time $\tau_{\text{rel}} = \tau_{\text{th}}/\pi^2$ where $\tau_{\text{th}} = L^2/\chi = 770\,\text{s}$ is the characteristic thermal time. More than 7 relaxations times, *i.e.* $t = 10\,\text{min}$, were allowed to system to establish a constant temperature gradient in the cell and then vibrations were applied. The measured on-board temperature field and computed vertical temperature profile $T(z)$ in the middle of the cell are shown in fig. 4 at the end of the first step. In fig. 4 we intentionally presented one experimental (a) and other numerical (b) graph to compare the temperature behavior in the middle of the cell. The isotherms are bent towards the corners because of the small grooves in the cell design. Due to the same reason the temperature profile in fig. 4b is not linear although the deviation is rather small.

4.1.1 Evolution of the temperature field on short time scale

At the second step, external vibrations are imposed to the cell perpendicular to the temperature gradient. We intend to investigate the temperature modification caused by the vibrational convection. Under external vibrations the fluid is set into motion. In case of high frequency (f)
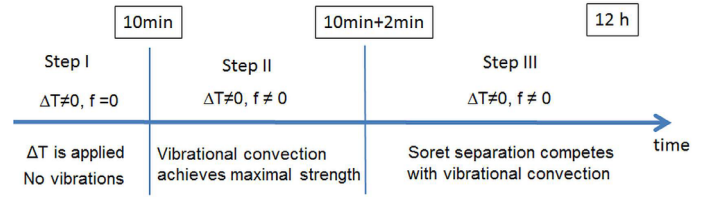

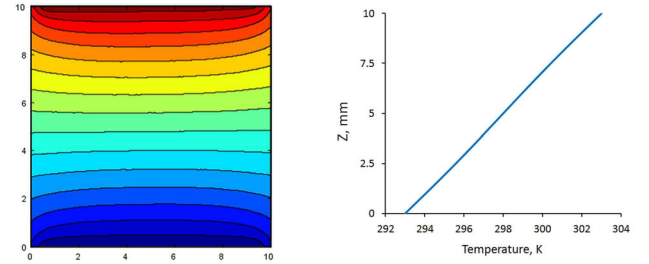**Fig. 3.** IVIDIL experimental scenario.

Fig. 4. Features of the temperature field at $t = 10\,\text{min}$ for mixture with $C_0 = 0.9$ when $\Delta T = 15\,\text{K}$. (a) Experimental isotherms; (b) computed profile $T(z)$ in the cell center.

vibrations and small amplitude (A), which was the case of the majority of IVIDIL experimental runs, each field can be decomposed into a "slow" time-averaged part (with a characteristic time much longer than $\tau_{\text{vib}} = 1/f$) and a "fast" oscillatory part (with a characteristic time τ) as $F = \overline{F} + F'$, for details see [1].

The time-averaged (mean) velocity, temperature and concentration were obtained from non-linear simulations by averaging over a few oscillation periods (n is the number of periods)

$$\overline{\mathbf{V}}(t) = \frac{1}{n\tau} \int\limits_{t}^{t+n\tau} \mathbf{V}(\tau')\,\text{d}\tau', \quad \overline{C}(t) = \frac{1}{n\tau} \int\limits_{t}^{t+n\tau} c(\tau')\,\text{d}\tau'. \quad (10)$$

The mean flow describes the non-linear response of the fluid to a periodic excitation and provides an independent mechanism of heat and mass transfer. The strength of mean flow is characterized by the Gershuni number [4,6] (known also as vibrational Rayleigh number, *e.g.*, see [1])

$$Gs = \frac{(A\omega\beta_T \Delta T L)^2}{2\nu\chi}.$$

The experimental observations showed that a significant mean flow is set within 2 minutes after imposing vibrations and later in time it varies weakly and slowly due to the Soret effect. In agreement with theoretical predictions [1], the IVIDIL experiment in a cubic cell revealed that in the absence of gravity the mean flow pattern consists of four vortices. The magnitude of the deviation of the temperature field caused by the mean flow from the stationary (conductive) one at the end of the first step is proportional to the vibrational forcing. For the experimental set of parameters the modification of the temperature field by vibration-induced convection was small. To analyze the temperature variations caused by the mean
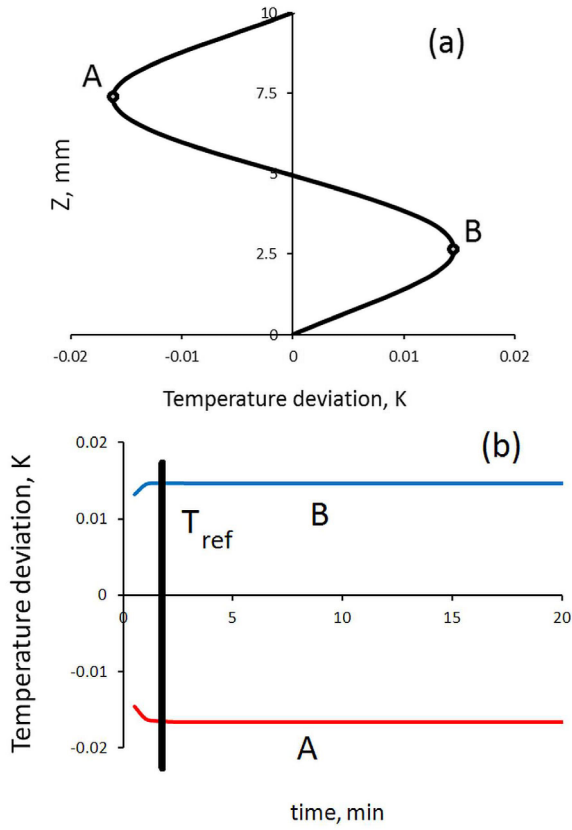
Fig. 5. Flow-induced temperature deviation from the conductive profile when $f = 1\,\mathrm{Hz}$, $A = 68\,\mathrm{mm}$, $\Delta T = 10\,\mathrm{K}$; (a) in the middle of the cell (Run 8); (b) the time history of the extrema in points A and B, *i.e.* $\delta T_{\mathrm{conv},\,A}(t)$ and $\delta T_{\mathrm{conv},\,B}(t)$.

flow, it is more illustrative to consider the temperature deviation from the conductive profile. Figure 5(a), which shows this temperature deviation along the central line of the cell, demonstrates that the mean flow makes the fluid at the upper part cooler and in lower part hotter than in the conductive state. However, these deviations are not symmetrical due to the temperature-dependent viscosity. The magnitude of the minima on the hot side at the point A, $\delta T_{\mathrm{conv},\,A} = T - T_{\mathrm{cond}} = -0.0166$, is larger than the maxima at the cold side $\delta T_{\mathrm{conv},\,B} = 0.0145$. The transient evolution of both local extrema is presented in fig. 5(b) and it specifies that time interval during which the temperature field reaches steadiness is less than two minutes ($t = 2\,\mathrm{min}$ is shown by vertical line).

In the picture processing of the IVIDIL experiment it was assumed that in later time the temperature remains constant and its distribution at the end of the second step, *i.e.* $t_{\mathrm{ref}} = 10\,\mathrm{min} + 2\,\mathrm{min}$, was taken as reference image. It means that in eq. (1) the first term on the right-hand side remains constant at later times

$$\Delta n_T = \left(\frac{\partial n}{\partial T}\right)_{p,c} \Delta T(x, z, t > t_{\mathrm{ref}}) = \mathrm{const.} \quad (11)$$

Consequently, all the variations of the refractive index at $t > t_{\mathrm{ref}}$ are attributed to the concentration change.

However during step three, which lasts 12 h, the vibrational force acted simultaneously with the Soret ef-
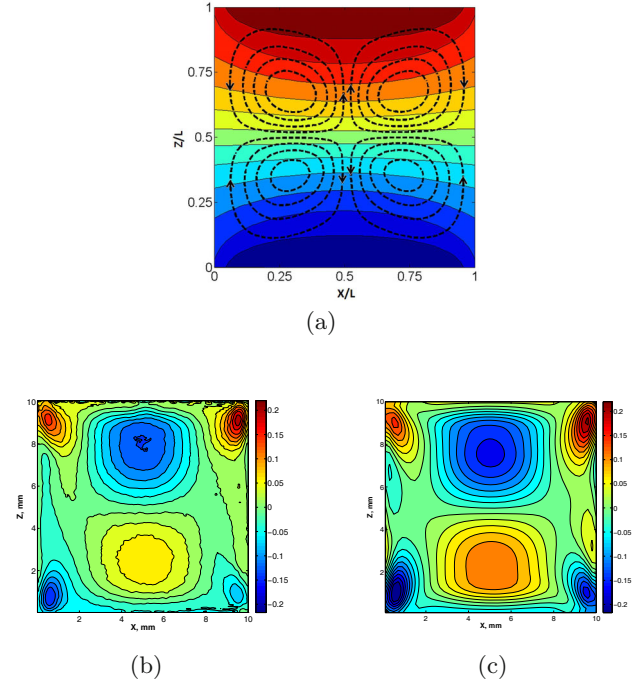
fect. The Soret effect leads to concentration variations and hence variations in density on the diffusion time scale. The mean flow, the result of the effect of vibrational force on density inhomogeneities, is slowly transformed and, in turn, modifies the temperature field. Note that the time interval in fig. 5(b) is limited by 20 min and it is insufficient for development of a process controlled by diffusion. Two questions emerge:

1) How strong is the modification of the temperature field on the long time scale?
2) Do we need second experimental diagnostic to separate contributions of temperature and concentration over the duration of the experiment?

4.1.2 Validation of the numerical model against experiment

The results of numerical simulations could help to answer these questions. The computed temperature field and isolines of the stream function of the mean flow are shown in fig. 6(a) two minutes after application of vibrations. The isolines clearly indicate the four-vortex flow pattern. To validate the numerical model against the experimental observation in convective state, the deviation of the temperature field from a conductive state is compared in the entire cross-section in fig. 6(b) and (c) at the same time instant. The small asymmetry of hot and cold spots about the horizontal mid-plane is attributed to the effect of temperature-dependent viscosity. The temperature patterns yielded by
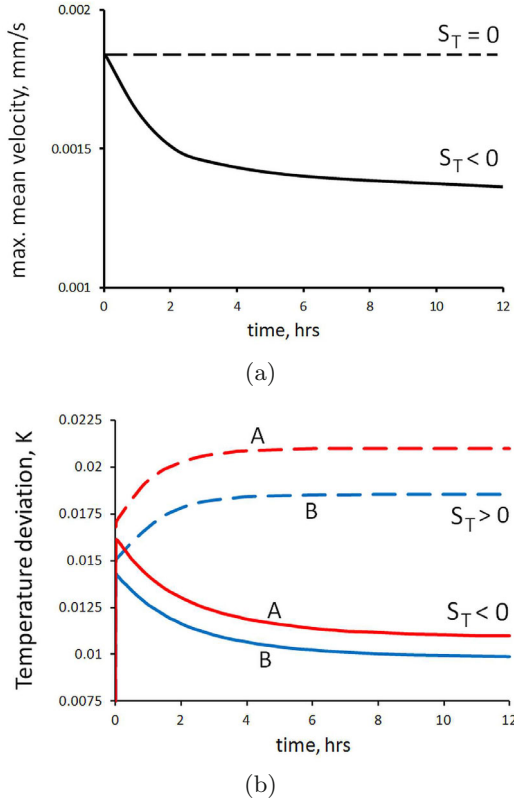

Fig. 6. Flow pattern 2 min after the start of vibrations, $t = t_{\mathrm{ref}}$. (a) The temperature field and isolines of the mean flow. (b) Experimental and (c) numerical deviation of the mean temperature field from the conductive state; results are shown in the XZ-plane when $Gs = 1982$, Run 15.

(a)

(b)

Fig. 7. (a) Evolution of the maximum of the mean velocity with time when $S_T = 0$ (dashed line) and $S_T = -7.4 \cdot 10^{-3}$ 1/K (solid line). Other parameters are $f = 1$ Hz, $A = 68$ mm, $\Delta T = 10$ K (Run 8 of IVIDIL). (b) Evolution of the temperature deviation from a conductive state on the long time scale (in point A the absolute value is plotted). The parameters are the same as for (a) but in the case of positive Soret the sign is changed for parametric study, $S_T = 7.4 \cdot 10^{-3}$ 1/K.

the experiment and numerical modelling are practically identical, except for minor differences in the structure of the isotherms near the lateral walls. This inspires confidence in the predictions of the numerical model.

4.1.3 Evolution of the temperature field on large time scale

Here we focus on the long-time evolution of mean flows in a system subjected to external vibrations, which can modify the temperature field. Short-time microgravity experiments without the Soret effect (in pure isopropanol) in the same cell as in IVIDIL have shown [6] that the mean flows achieve a sustained flow pattern in ~ 20 s. Our numerical results are consistent with short-time experiments. The results of long-time simulations for $S_T = 0$, $S_T > 0$ and $S_T < 0$, are presented in fig. 7. The dashed line in fig. 7(a) shows that the maximum of the mean velocity created within less than two minutes remains constant over 12 hours when $S_T = 0$. However, in the case of negative Soret (solid line), the maximum of the mean velocity reveals the highly transient behaviour. Over time, the negative Soret effect leads to diminishing

of the density gradients which drive the mean flow. The strongest mean flow was formed during step II (at the first 2 min) and its maximum velocity was $\overline{V}_{\max} \approx 18\,\mu$m/s. Within the following 12 h the maximum velocity diminished down by 30%, *i.e.* to $\overline{V}_{\max} \approx 13\,\mu$m/s. The decreasing rate is larger in the first hours.

Consequently, the variation of the mean flow causes additional modification of the temperature field. Figure 7(b) shows deviation of the temperature field from a conductive state (let us denote δT) over 12 h along the central line of the cell $x = L/2$. Notations A and B introduced in fig. 5(a) are used here. Note that evolution in point A is shown as absolute value to emphasize the difference between the upper and lower part, which is assigned to temperature-dependent viscosity. It can be seen that solid curves ($S_T < 0$) exhibit a well-defined extremum at the very beginning, $t \sim t_{\text{ref}}$. In the case of negative Soret the deviations decrease over time approaching the asymptotic values $|\delta T_{\text{conv}, A}| = 0.095$ and $\delta T_{\text{conv}, B} = 0.0115$. We have also carried out a similar analysis of the flow with $S_T > 0$ simply changing sign of S_T while other parameters are kept the same. Figure 7(b) reveals that the positive Soret effect increases the net density gradients and this leads to the growth of the magnitude of the mean flow and temperature deviations from the conductive state. Thus, by the end of this section we demonstrated that temperature modifications on the long time scale are present but they were not taken into account in the variations of the refractive index.

4.1.4 Impact of the temperature variations on the large time scale on the accurate processing of the concentration field

The purpose of this section is to check the quantitative agreement between two cases of image processing: neglecting or considering changes of a temperature field caused by a mean flow during step III. The measured optical phase $\Delta\varphi(x, z, t)$ in eq. (1) is an additive value, then the total variation of a refractive index can be written as the sum of three temperature contributions at different time steps and concentration

$$
\begin{aligned}
\Delta n(x, z, t) &= \Delta n_T + \Delta n_C \\
&= \Delta n_T^{\mathrm{I}}(x, z, t) + \Delta n_T^{\mathrm{II}}(x, z, t) \\
&\quad + \Delta n_T^{\mathrm{III}}(x, z, t) + \Delta n_C. \tag{12}
\end{aligned}
$$

The sum of the first two terms provides variation of the refractive index at the reference image and remains constant at $t > t_{\text{ref}}$. We have shown in the previous section that the third term is a non-zero quantity which slowly changes in time. From eq. (12) the net variation of the refractive index during step III can be written as

$$
\begin{aligned}
\Delta n(x, z, t)^{\mathrm{III}} &= \Delta n(x, z, t) - \Delta n_{\text{ref}} \\
&= \Delta n_T^{\mathrm{III}}(x, z, t) + \Delta n_C(x, z, t). \tag{13}
\end{aligned}
$$

Let us estimate the possible contribution of the term $\Delta n_T^{\mathrm{III}}$ in the concentration field on the step III considering that
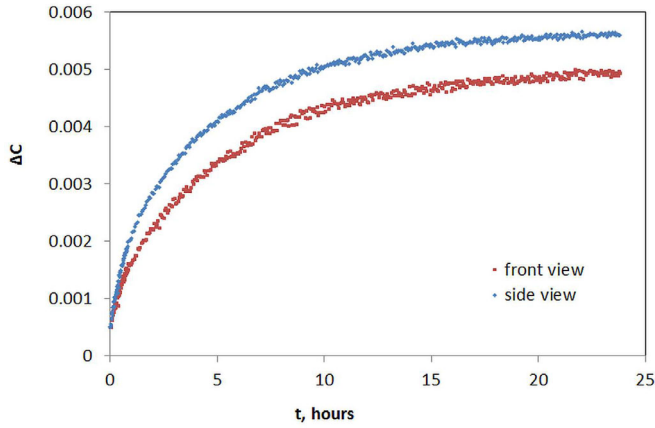
Fig. 8. Experimentally observed Soret separation in time in two perpendicular views (Run 8_{ext} of IVIDIL) when $f = 1\,\text{Hz}$, $A = 68\,\text{mm}$, $\Delta T = 10\,\text{K}$, $Gs = 541$.

Fig. 9. Evolution of temperature deviation from the conductive state on the cold side when $f = 2\,\text{Hz}$, $A = 61\,\text{mm}$, $\Delta T = 15\,\text{K}$, $Gs = 1982$ (Run 15 of IVIDIL).

$\Delta n_T^{\text{III}}(x, z, t) = \Delta n_C^{\text{III}}(x, z, t)$. Then

$$\left(\frac{\partial n}{\partial T}\right)_{p,c} \delta\tilde{T}(x, z, t > t_{\text{ref}}) = \left(\frac{\partial n}{\partial c}\right)_{p,T} \Delta\tilde{C}(x, z, t)^{\text{III}}, \tag{14}$$

here $\delta\tilde{T}$ is the deviation of the temperature from that which was at the end of the step II (from δT shown in fig. 7(b)) and $\Delta\tilde{C}(x, z, t)^{\text{III}}$ is the expected variation of the concentration caused by $\delta\tilde{T}$. Taking the values of contrast factors from table 1, the possible concentration addition is

$$\Delta\tilde{C}(x, z, t)^{\text{III}} = \left(\frac{\partial n}{\partial T}\right) \Big/ \left(\frac{\partial n}{\partial c}\right) \delta\tilde{T}$$

$$= 9.544 \cdot 10^{-3}\, \delta\tilde{T}. \tag{15}$$

The thermal contrast factor $\partial n/\partial T$ is two orders of magnitude smaller than the concentration contrast factor $\partial n/\partial C$ and it reduces the impact of the temperature variations on the concentration field. The measured separation of the component during an extended (24 hours) experimental run of IVIDIL is shown in fig. 8 in two perpendicular views. The maximal value of the Soret separation in the side view is $\Delta C = C - C_0 \approx 0.0056$ while the maximal temperature deviation over step III is $\delta\tilde{T} \approx 0.006$ as follows from fig. 7(b). Consequently, substituting these values into eq. (15) we obtain

$$\Delta\tilde{C}(x, z, t)^{\text{III}} = 9.544 \cdot 10^{-3}\, \delta\tilde{T} = 5.7264 \cdot 10^{-5}$$

and

$$\frac{\Delta\tilde{C}(x, z, t)^{\text{III}}}{\Delta C} \cdot 100\% \approx 1\%. \tag{16}$$

We can draw the conclusion that in the case when images of the experiment IVIDIL are processed neglecting the temperature changes after selection of a reference image, an error at concentration separation is about 1% for moderate Gershuni numbers. This error is comparable with
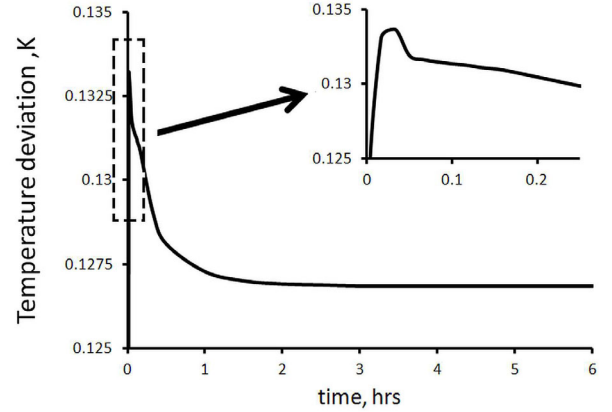

Fig. 10. Experimentally observed Soret separation in time in two perpendicular views when $f = 2\,\text{Hz}$, $A = 62\,\text{mm}$, $\Delta T = 15\,\text{K}$, $Gs = 1982$ (Run 15 of IVIDIL).

experimental errors. The study is done for $Gs = 541$ and with the increase of the vibrational forcing, *i.e.* with the increase of Gs number, the error may slightly increase.

To resolve this issue we have also analyzed the temperature deviation for the case of large Gershuni number, $Gs = 1982$ (Run 15). Indeed, the insert in fig. 9 demonstrates the formation of a strong mean flow in the first 1–2 min which leads to large perturbations of temperature field. The maximal temperature deviation at $Gs = 1982$ is nine times larger than at $Gs = 541$, compare $\delta T = 0.133$ (fig. 9) against $\delta T = 0.0145$ (fig. 7(b)). However, the long time history in fig. 9 does show only small modifications of the temperature field after $t = t_{\text{ref}}$. As a result, the deviation of the temperature at later time for $Gs = 1982$ is the same, $\delta\tilde{T} = 0.006$, as for smaller Gershuni number, $Gs = 541$.

The negative Soret effect decelerates the development of the mean flow by reducing the density gradients. On the contrary, the increase of vibrational forcing leads to
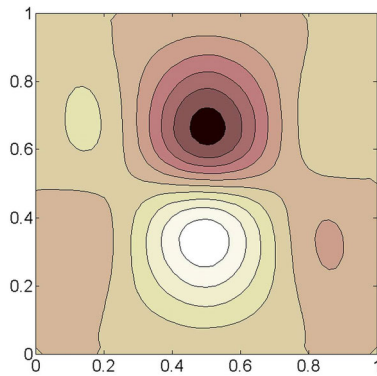
Fig. 11. Snapshot ($t = 12$ h) of a spatial distribution of the concentration field $\Delta\tilde{C}(x, z, t)^{\text{III}}$ caused by the convective perturbations of the temperature field within step III.

a stronger mean flow and a decrease of the Soret separation. Actually, at large vibrational forcing the mass transfer regime changes from diffusive to convective. Figure 10 shows the time evolution of the Soret separation at strong vibrational forcing, $Gs = 1982$, measured on board of the ISS. The large difference in the separation between two perpendicular views also indicates a strong mean flow which re-mixes fluid. It follows that $\Delta C \approx 0.00129$ is about five times smaller than at $Gs = 541$. Following our target which is to calculate an error in image processing, we apply the same consideration as in eq. (16)

$$\Delta\tilde{C}(x, z, t)^{\text{III}} = 9.544 \cdot 10^{-3}\ \delta\tilde{T} = 5.7264 \cdot 10^{-5}$$

and

$$\frac{\Delta\tilde{C}(x, z, t)^{\text{III}}}{\Delta C} \cdot 100\% \approx 4.4\%. \qquad (17)$$

So, the coupling of thermal and convective phenomena provides the maximal error in the determination of the concentration field smaller than 5%.

We have also determined the spatial distribution of the *overestimated* concentration field $\Delta\tilde{C}(x, z, t)^{\text{III}}$ at the end of the experiment, at $t = 12$ h, which is shown in fig. 11. Note that the above-obtained magnitude of the error from 1% to 5% is the maximal value over the entire cross-section which attains only inside the centers of the large spots in fig. 11. This suggests that neglecting the modification of the temperature field after the selection of the reference image at the end of step II does not considerably affect the correctness of the resulting concentration field.

5 Conclusions

We have presented experimental and numerical studies of heat and mass transfer in a binary mixture with Soret effect subjected to controlled vibrations. The experiments were conducted in the microgravity environment of the ISS in the frame of the experiment IVIDIL. A cubic cell

with differentially heated walls was filled with a water-isopropanol mixture and subjected to a translational vibration in the direction perpendicular to the temperature gradient. The stationary temperature field is reached within a few thermal times (~ 10 min) while the concentration field requires dozens of hours. The experimental observations revealed that a significant mean flow is set within 2 minutes after imposing vibrations and later in time it varies weakly and slowly due to the Soret effect. The associated perturbations of the temperature field may also vary at later time. Usually these temperature modifications are not taken into account in picture processing at later time. A mathematical model has been developed to verify the accuracy of picture processing based on the classical approach used in non-convective systems with the Soret effect.

We have performed a quantitative check of the consistency between two cases of image processing: neglecting or considering changes of a temperature field caused by a mean flow after selection of the reference image. The study was conducted for low and strong vibrational forcing. Our results indicate that the reference image has to be selected after the time moment when the strength of vibrational convection has passed its initial extremum; for the considered system it is about 2 min after imposing the vibrations. The analyses showed that the neglect of convective temperature perturbation at a later time does not considerably affect the accuracy of the optically measured concentration field.

Obviously, the conclusion about the small error in image processing is valid for vibrational flows when the velocity of the mean flow is about a few microns per second. It may not be true for other types of convective flows, and then, a second diagnostics, for example the second light source with a different wavelength, will be required.

References

1. G.Z. Gershuni, D.V. Lyubimov, *Thermal Vibrational Convection* (Wiley and Sons, Berlin, 1998).
2. Z. Gershuni, A.K. Kolesnikov, J.C. Legros, B.I. Myznikova, J. Fluid Mech. **330**, 2561 (1995).
3. D. Beysens, Micrograv. Sci. Technol., DOI: 10.1007/s12217-014-9373-1 (2014).
4. A. Mialdun, I. Ryzhkov, D. Melnikov, V. Shevtsova, Phys. Rev. Lett. **101**, 084501 (2008).
5. V. Shevtsova, Yu. Gaponenko, D. Melnikov, I. Ryzhkov, A. Mialdun, Acta Astronaut. **66**, 166 (2010).
6. V. Shevtsova, I. Ryzhkov, D. Melnikov, Yu. Gaponenko, A. Mialdun, J. Fluid Mech. **648**, 53 (2010).
7. A.V. Zyuzgin, A.I. Ivanov, V.I. Polezhaev, G.F. Putin, E.B. Soboleva, Cosmic Res. **39**, 175 (2001).

8. A.V. Zyuzgin, G.F. Putin, N.G. Ivanova, A.V. Chudinov, A.I. Ivanov, A.V. Kahnykov, V.I. Polezhaev, V.M. Emelianov, Adv. Space Res. **32/2**, 205 (2003).
9. D. Beysens, Europhys. News **37**, 22 (2006).
10. Y. Garrabos, D. Beysens, C. Lecoutre, A. Dejoan, V. Polezhaev, V. Emelianov, Phys. Rev. E **75**, 056317 (2007).
11. S. Mazzoni, V. Shevtsova, A. Mialdun, D. Melnikov, Yu. Gaponenko, T. Lyubimova, M.Z. Saghir, Europhys. News **41**, 14 (2010).
12. V. Shevtsova, T. Lyubimova, Z. Saghir, D. Melnikov, Yu. Gaponenko, V. Sechenyh, J. C. Legros, A. Mialdun, J. Phys.: Conf. Ser. **327**, 012031 (2011).
13. V. Shevtsova, A. Mialdun, D. Melnikov, I. Ryzhkov, Y. Gaponenko, Z. Saghir, T. Lyubimova, J.C. Legros, C. R. Mec. **339**, 310 (2011).
14. A. Mialdun, V. Yasnou, V. Shevtsova, A. Koeniger, W. Koehler, D. Alonso de Mezquia, M.M. Bou-Ali, J. Chem. Phys. **136**, 24 (2012).
15. A. Mialdun, V. Shevtsova, C. R. Mec. **339**, 362 (2011).
16. A. Mialdun, V. Shevtsova, J. Chem. Phys. **134**, 044524 (2011).
17. M. Bou-Ali, private communication (2011).
18. D.V. Lyubimov, Eur. J. Mech. B/Fluids **14**, 439 (1995).